ChemComm

ROYAL SOCIETY OF CHEMISTRY

HIGHLIGHT

View Article Online
View Journal | View Issue

Cite this: *Chem. Commun.*, 2025, **61**, 15510

Carbon aerogels and xerogels: next-generation materials for sustainable energy and environmental solutions

David Tomić, [a] Kristina Radinović, [a] Dušan Mladenović, [a] Jadranka Milikić, [a] Diogo M.F. Santos, [b] Armando J. L. Pombeiro, [c] Anup Paul *[d] and Biljana Šljukić *[ab]

Received 30th April 2025,
Accepted 26th August 2025

DOI: 10.1039/d5cc02477c

rsc.li/chemcomm

Carbon aerogels and xerogels, with their 3D porous architectures, ultralow density, high surface area, and excellent conductivity, have emerged as multifunctional materials for energy and environmental applications. This review highlights recent advances in the synthesis of these materials *via* polymerisation, drying, and carbonisation, as well as the role of novel precursors such as graphene, carbon nanotubes, and biomass. Emphasis is also placed on doped and metal-decorated carbon gels as efficient electrocatalysts for oxygen reduction reactions, enabling four- and two-electron pathways for energy conversion and the production of green H_2O_2, respectively. Aerogels' high specific capacitance and stability also position them as promising materials for supercapacitors. The versatility of carbon aerogels and xerogels offers exciting prospects for future innovations in catalysis, energy storage, and sustainable technologies.

1. Introduction

Carbon aerogels and xerogels have emerged as distinct classes of highly porous 3D carbon-based materials, offering ultralow densities (<0.1 g cm^{-3}), high specific surface area (500–2000 m^2 g^{-1}), and excellent electrical conductivity (10–100 S cm^{-1}).[1–3] Originating from Pekala's pioneering work on aerogels from resorcinol–formaldehyde precursors, their development has been significantly advanced by integrating graphene, carbon nanotubes (CNTs), and biomass-derived materials.[4–15]

One of the most promising applications of carbon aerogels and xerogels is in energy storage systems, particularly as electrode materials for supercapacitors.[10,14] Their high surface area, porosity, and electrical conductivity enable efficient charge storage and rapid charge/discharge cycling. Doping strategies using nitrogen, sulfur, or transition metals (*e.g.*, cobalt, nickel, iron) have enhanced electrochemical performance, achieving specific capacitances >400 F g^{-1} in supercapacitors, making them competitive with traditional materials.[16,17]

Carbon aerogels and xerogels have also shown significant potential as electrocatalysts for the oxygen reduction reaction (ORR), a critical process in fuel cells and metal–air batteries.[18,19] As ORR catalysts, doped and metal-decorated aerogels offer a cost-effective alternative to Pt-based systems, supporting both four- and two-electron pathways, which are key for fuel cells and sustainable H_2O_2 production, respectively. Their high surface area and catalytic activity also facilitate the removal of pollutants in environmental applications.[20] This review summarises recent advances in synthesis strategies, structure–property relationships, and multifunctional applications of carbon aerogels and xerogels, highlighting their promise in next-generation sustainable technologies.

2. Synthesis of carbon aerogels and xerogels

The first ever aerogel, based on silica (SiO_2), was produced by Kistler in the 1930s, with the second generation of silica gels being introduced in the 1970s.[3] The first organic aerogels based on resorcinol and formaldehyde were synthesised by Pekala in

[a] *University of Belgrade-Faculty of Physical Chemistry, Studentski trg 12-16, Belgrade, Rebublic of Serbia*
[b] *Center of Physics and Engineering of Advanced Materials, Laboratory of Physics for Materials and Emerging Technologies, Chemical Engineering Department, Instituto Superior Técnico, Universidade de Lisboa, Lisbon, 1049-001, Portugal. E-mail: biljana.paunkovic@tecnico.ulisboa.pt*
[c] *Centro de Química Estrutural, Instituto Superior Técnico, Universidade de Lisboa, Av. RoviscoPais, 1049-001 Lisboa, Portugal*
[d] *Centro de Estudos de Engenharia Química, Instituto Superior de Engenharia de Lisboa, Instituto Politécnico de Lisboa, Lisboa, Portugal. E-mail: kanupual@gmail.com*

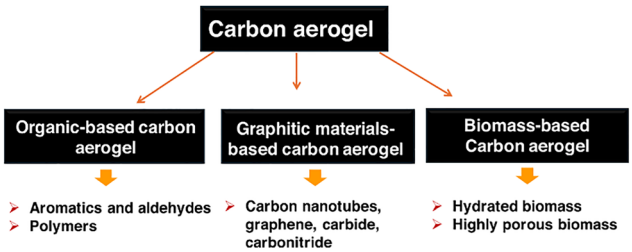

Fig. 1 Classification of carbon aerogels. The synthesis of carbon aerogels involves three key steps: polymerisation, drying, and carbonisation.

the 1990s.[12] Subsequently, organic aerogels were synthesised using various precursors such as aldehydes, poly(vinyl alcohol or chloride), polyimides, and hydroxybenzenes. Pyrolysis of these organic aerogels in an inert atmosphere resulted in the formation of carbon aerogels. In the 2010s, novel carbon aerogels with graphene, CNT, carbide, and carbonitride aerogels were synthesised (Fig. 1).[10,21]

2.1. Polymerisation

The synthesis begins with polymerisation, where a hydrogel network is formed through three sequential steps (Fig. 2). The first step is an addition reaction, which introduces hydroxymethyl groups (–CH_2OH) from aldehydes and hydroxyl groups. Then, condensation reactions of –CH_2OH groups lead to the formation of methylene (–CH_2–) and methylene ether (–CH_2OCH_2–) bridges. Ultimately, the crosslinking and agglomeration of the obtained products result in a 3D hydrogel structure.[5,10] The addition step typically begins with the addition of alkaline catalysts, such as calcium hydroxide ($Ca(OH)_2$), potassium carbonate (K_2CO_3), sodium hydroxide (NaOH), and sodium carbonate (Na_2CO_3).[5,10] These bases catalyse the electrophilic addition reaction between formaldehyde and resorcinol.[22,23] Namely, in these conditions, the resorcinol anions with strong nucleophilic addition could be formed,[22,23] allowing them to react with resorcinol and form hydroxymethyl groups. These groups then condense into methylene and methylene-ether bridges, gradually building a polymer network.[5] As crosslinking continues, a 3D hydrogel structure takes shape. To enhance the material's properties, additives

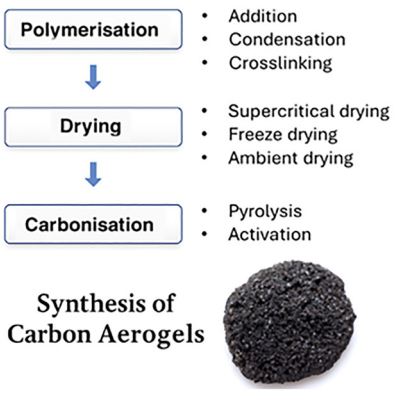

Fig. 2 Procedure for the preparation of carbon aerogels.

such as inorganic salts, ceramic nanoparticles or polymer templates are often used, contributing to the aerogel's ordered porous structure, a narrow pore size distribution and mechanical flexibility.[13,24,25]

Different organic aerogels can also be prepared by combining formaldehyde with phenol, cresol, melamine, and other compounds.[5,10] More recently, sustainable precursors like CNTs, graphene, cellulose, and lignin have been explored, offering greener pathways to high-performance carbon aerogels and xerogels.[1,4,6,7]

In addition to organic-based carbon aerogels, graphitic material-based and biomass-based carbon aerogels have recently been synthesised and investigated for many applications. Namely, precursors such as carbon nanotubes (CNTs), graphene, and biomass are proposed as alternatives to polymers for more practical synthesis.[1,4–6,26,27]

2.2. Drying

The drying method plays a critical role in retaining the pore structure of carbon aerogels. Supercritical drying, typically using CO_2, eliminates liquid–gas interfaces, thereby preserving over 90% of the porosity.[8,10] However, it requires expensive equipment and careful control. Freeze-drying, on the other hand, involves the sublimation of the solvent under low pressure, producing ice-templated pores. The resulting pore size depends on the freezing rate and precursor concentration. Ambient drying is the most cost-effective method, but often leads to significant structural shrinkage (over 10%) due to capillary forces. This shrinkage can be minimised through solvent exchange, commonly with acetone. Supercritical drying yields the highest surface areas (often exceeding 1000 $m^2\ g^{-1}$), while freeze-drying balances structural integrity and scalability.

On the other hand, xerogels are formed by drying a gel at ambient pressure, which causes shrinkage and collapse of the pore structure. In contrast, aerogels, particularly those produced *via* supercritical drying, preserve a highly porous and lightweight framework.[6–8] Although aerogels offer superior porosity, xerogels are more commercially viable due to their simpler production process and lack of complex equipment requirements. Recent advances have enabled the superfast synthesis of carbon xerogels,[11] achieving high surface areas and pore volumes within just 5 hours through hydrothermal gelation and direct carbonisation, eliminating lengthy drying steps without compromising performance.

2.3. Carbonisation

During carbonisation, pyrolysis at 773 to 2773 K under an inert atmosphere (nitrogen (N_2) or argon (Ar)) converts the organic gel into a conductive sp^2-carbon matrix. Release of hydrogen (H_2) and oxygen (O_2) gases during carbonisation leads to a porous and carbonised 3D network. Thus, pyrolysis enhances both mechanical stability and electrical conductivity, allowing the microporous properties of the aerogels to be modified.[28] Still, at higher temperatures (above 1473 K), the surface area tends to decrease, and beyond 2273 K, graphitisation occurs.[9,11,15] Complete graphitisation of aerogel provides its

high electrical conductivity.[9,11] Choosing the appropriate pyrolysis temperature results in carbon aerogels of high specific surface area and electrical conductivity.[9,11,15]

Physical and chemical activation treatments of carbon aerogels using carbon dioxide (CO_2), potassium hydroxide (KOH), NaOH or steam are often applied to further tailor the textural properties of aerogels, including pore volume, pore size distribution, and specific surface area.[29] Carbon aerogels and xerogels can be engineered for specific applications with desired structural and functional properties by carefully optimising the carbonisation and activation steps. The synthesis of carbon aerogels and xerogels for tailoring their properties to specific applications is described and illustrated throughout this review paper, along with their electrochemical performance.

2.4. Synthesis of novel carbon aerogels and their composites

As mentioned, aerogel could also be synthesised using carbon-based materials such as graphene,[2,30] graphene oxide (GO),[31] and CNT.[32] Herein, a few examples of novel syntheses of carbon (graphite) aerogels are presented. Moreover, different composites are nowadays being synthesised for particular applications.

Carbon aerogel composed of self-assembled nanosheets with short-range graphitic structures was prepared using a dual graphitisation approach, *i.e.*, Fe-catalysed graphitisation combined with graphene oxide-induced graphitisation.[33] Agar, ferric nitrate ($Fe(NO_3)_3$), and GO were used as the carbon precursor, as the catalyst, and as the initiator of the noted synthesis, respectively. A polysaccharide agar was well-dispersed in water at high temperature, followed by the addition of $Fe(NO_3)_3$ solution to obtain Fe^{3+}–agar complex. Next, urea as a nitrogen source and GO were added and stirred at a temperature of 90 °C for 5 h. A hydrogel was prepared by naturally cooling the dispersion to ambient temperature and then transformed into an Fe–agar/GO aerogel through freeze-drying. Subsequent carbonisation of the aerogel at 800 °C for 2 h resulted in a carbon aerogel with carbon nanosheets. Prepared CA-x (x = 0, 0.1, 0.2, 0.3 g of GO) with many short graphitic structures and appropriate micropore sizes, were explored as a hard carbon anode material for Na^+ storage.[33]

The synthesis of carbon aerogel for piezoelectric pressure sensors began with the fabrication of silver-loaded carbonised hollow polyacrylonitrile nanofibers (Ag@HCNF) *via* electrostatic spinning. This was followed by mixing Ag@HCNF with a graphite aqueous solution after heat treatment, and then freeze-drying.[1] Ag@HCNF and graphite or graphene were coupled using a silicone coupling agent (KH-550), creating a dispersion. Then, polyethylene glycol and polyethylene pyrrole were added to the dispersion to improve the 3D networking, while borax and glutaraldehyde were added as cross-linking agents. The obtained product was then freeze-dried for 24 h to obtain carbon aerogel with a 3D porous structure and a density of 18.07 mg cm^{-3}; this carbon aerogel can be placed on petals without deformation.[1]

Graphite aerogels (GAs) can also be used as 3D support matrices for the preparation of composite materials. For instance, polyethylene glycol composite phase change materials (CPCM) were prepared by starting from a waste material, ground tire rubber (GTR).[27] GTR powder was initially used to prepare aerogels by freeze-drying. Two solutions were prepared by dissolving and stirring GTR powder with GA in acetone, and GTR powder with polyvinyl alcohol in deionised water to form a gel-like solution. The two prepared solutions were mixed, and then activated carbon or expanded graphite was added. The mixture was first frozen in a refrigerator and then freeze-dried to create aerogel. This aerogel, serving as a 3D support matrix, was next impregnated with polyethylene glycol *via* a vacuum impregnation method, and CPCM was obtained. CPCM exhibited strong thermal reliability and excellent shape stability and thus can be used in thermal energy storage applications.[27]

Synthesis of other composite materials based on graphite aerogels, such as self-standing 3D rose-like nitrogen-doped graphite aerogels modified with bimetallic oxides ($FeNiO_x$@N/GA), was also reported.[26] Firstly, self-standing 3D flower-shaped graphite aerogels modified with bimetallic layered double hydroxide (FeNi LDH@GA) were prepared by a simple hydrothermal method and freeze-drying for 72 h. In this step, FeNi layered double hydroxide (FeNi LDH) is prepared on the graphene hydrogels. Then, graphite aerogels modified with 3D flower-shaped bimetallic metal–organic frameworks (MOF) (FeNi MOF@GA) were prepared by a high-temperature reaction at 350 °C for 2 h in a N_2 atmosphere. This second step involves the coordination of terephthalic acid with FeNi LDH to form a 3D FeNi MOF@GA. Finally, nitrogen-doped 3D flower-like bimetallic oxide-modified graphite aerogels ($FeNiO_x$@N/GA) were synthesised by a high-temperature reaction at 350 °C for 2 h in N_2 atmosphere.[26] In the last step, dicyandiamide is added to FeNi MOF@GA, resulting in the formation of $FeNiO_x$@N/GA.[26] The obtained aerogel material had an excellent pressure resistance, tested using weights that exceeded the obtained mass nearly 200 times.[26]

3. Applications for sustainable energy

3.1. Carbon aerogels and xerogels for oxygen reduction reaction

The oxygen reduction reaction is a key process in fuel cells and metal–air batteries, where O_2 is reduced to water or hydroxyl ions (OH^-), depending on the electrolyte media. However, its slow kinetics limit the device efficiency. While platinum (Pt)-based catalysts are effective, their high cost and scarcity hinder commercial viability. This has driven the search for low-cost, eco-friendly, and earth-abundant alternatives to replace Pt in ORR applications.[34] The above-discussed versatility has facilitated the development of numerous cbon aerogel-based materials for ORR catalysis, serving as catalysts or as adequate supports for ORR active metal nanoparticles.

The ORR on a catalyst surface can typically proceed *via* two distinct pathways. The four-electron reduction pathway is

preferred for energy storage and conversion applications. In contrast, the two-electron pathway, while less favourable in such systems, is useful for hydrogen peroxide (H_2O_2) production and other specialised applications, as discussed below.

The four-electron mechanism of oxygen reduction represents the complete reduction of molecular O_2 to H_2O in acidic media (eqn (1)) or to OH^- in alkaline media (eqn (2)) *via* transfer of four electrons.[35]

$$4e^- \text{ pathway (acidic)} \quad O_{2,ads} + 4H^+ + 4e^- \rightarrow 2H_2O; \quad E^0 = +1.229 \text{ V } \textit{vs.} \text{ SHE} \tag{1}$$

$$4e^- \text{ pathway (alkaline)} \quad O_{2,ads} + 2H_2O + 4e^- \rightarrow 4OH^-; \quad E^0 = +0.401 \text{ V } \textit{vs.} \text{ SHE} \tag{2}$$

where E^0 is the standard electrode potential *versus* the standard hydrogen electrode (SHE) at 25 °C.[36] The above equations represent the overall ORR in two media. However, ORR is a multi-electron and multi-step process that includes a series of intermediate species.

The structure of the double layer that forms at the electrode–electrolyte interface plays a crucial role in ORR catalysis.[37] In the alkaline media, H_2O molecules act both as a solvent and the source of the protons during ORR. This means that the inner Helmholtz plane is populated by chemisorbed O_2, H_2O dipoles, and adsorbed OH^- species. The outer Helmholtz plane is populated with alkali metal ions, which are typically well-solvated. The four-electron mechanism involves the strong chemisorption of molecular O_2 at the inner sphere (eqn (3)), followed by a $4H^+/4e^-$ transfer (eqn (4) and (5)). Unlike in the alternative two-electron pathway, here all the reaction intermediates remain adsorbed on the electrode surface until the final products are formed. Only then the products are desorbed from the surface into the bulk electrolyte.[38]

$$O_2 \rightarrow O_{2,ads} \tag{3}$$

$$O_{2,ads} + H_2O + 2e^- \rightarrow (HO_2^-)_{ads} + OH^- \tag{4}$$

$$(HO_2^-)_{ads} + H_2O + 2e^- \rightarrow 3OH^- \tag{5}$$

The presented mechanism is the so-called associative mechanism, which does not involve the dissociation of molecular oxygen into two O* atoms. If the O_2 molecule dissociates into two O* occupying two different active sites *, which are then reduced, the mechanism is called the dissociative mechanism. Furthermore, if the chemisorbed H_2O is also present, some scientists propose a third mechanism which does not involve a transfer of e^-, therefore making these steps of ORR potential-independent.[39]

The mechanism of two-electron reduction can be presented by eqn (6) and (7):

$$2e^- \text{ pathway (acidic)} \quad O_2 + 2H^+ + 2e^- \rightarrow H_2O_2; \quad E^0 = +0.70 \text{ V } \textit{vs.} \text{ RHE} \tag{6}$$

$$* + O_2 + H^+ + e^- \rightarrow *OOH \tag{6a}$$

$$*OOH + (H^+ + e^-) \rightarrow H_2O_2 + * \tag{6b}$$

$$2e^- \text{ pathway (alkaline)} \quad O_2 + 2H_2O + 2e^- \rightarrow H_2O_2 + 2OH^-; \quad E^0 = +0.76 \text{ V } \textit{vs.} \text{ RHE} \tag{7}$$

where * represents a free active site, and *OOH represents the only adsorbate in the two-electron ORR.[40]

Two-electron and four-electron O_2 reduction pathways are competitive reactions; nonetheless, a specific mechanism can be promoted based on the reaction thermodynamics and the Sabatier principle. The volcano plot shows that there is a linear relationship between the binding strength of reaction intermediate *OOH to the electrocatalyst surface and the catalytic activity. Namely, the *OOH binding strength determines the ORR pathway; from the volcanic peak to the left ($4e^-$ pathway of H_2O formation) and from the volcanic peak to the right ($2e^-$ pathway of H_2O_2 formation).[40,41]

Establishing a clear and systematic correlation between microstructural features and electrochemical performance is vital for the rational design of high-performance materials used in batteries, supercapacitors, and other energy storage devices.[42] Critical microstructural parameters, including pore size distribution, hierarchical porosity, and particle size, directly influence charge transport, ion diffusion, and active site accessibility. Pore size plays a key role in ion transport and active sites accessibility. Micropores (<2 nm) offer a high surface area, which is beneficial for charge storage, but may limit ion mobility, especially at high rates. Mesopores (2–50 nm) provide efficient pathways for ion diffusion, thereby improving rate capability. Macropores (>50 nm) act as ion-buffering reservoirs, facilitating rapid ion transport across the electrode. A hierarchical porosity that integrates micro-, meso-, and macropores can maximise both energy and power densities by combining high surface area with fast ion transport and reduced diffusion resistance.[43]

Particle size also significantly affects electrochemical response. Smaller particles shorten the diffusion path for ions and electrons, increase surface area, and expose more active sites, thereby enhancing rate performance and capacity.[44,45] However, excessive size reduction may lead to particle agglomeration, instability, and lower packing density, which can negatively affect cycling stability.

BET analysis enables the determination of specific surface area and pore size distribution, while electrochemical impedance spectroscopy (EIS) provides insight into charge-transport and internal resistance. Electronic microscopy reveals particle size and shape. By linking these structural, textural, and morphological details with electrochemical performance data, we can build a more comprehensive picture and deepen our understanding of the ongoing processes essential for designing better materials and improving energy storage technologies.

To promote a specific ORR pathway, various surface functional groups can be deliberately introduced onto catalyst materials to favour either the four-electron or two-electron reduction mechanism. For example, the incorporation of pyridinic nitrogen at sp^2-hybridized carbon edge sites has been shown to enhance the four-electron pathway by providing active sites for O_2 adsorption and facilitating the breaking of O–O

bond.[46] Conversely, the presence of oxygen-containing groups such as carboxyls at defect sites or edges tends to favour the two-electron pathway, as these groups are less effective in breaking the O–O bond, thereby promoting the formation of H_2O_2.[47] Some functional groups, such as pyrrolic nitrogen, exhibit lower selectivity and may participate in both two- and four-electron ORR without strong selectivity for either.[48,49]

The selective promotion of a desired electrochemical reduction pathway can also be effectively achieved through the appropriate choice of electrolyte and pH adjustment. In acidic media, the choice of ORR electrocatalysts is generally limited to Pt and Pt-based ones, which exhibit high intrinsic activity and stability. In contrast, an alkaline environment generally enhances ORR activity, particularly when employing non-precious metal catalysts. However, in acidic conditions, the reaction typically proceeds *via* a four-electron reduction mechanism to form H_2O, while many non-platinum group metal catalysts in alkaline media tend to favour the two-electron pathway, resulting in the formation of H_2O_2.[50] Under neutral pH conditions, both pathways may coexist, with the product distribution influenced by the nature of the electrocatalyst and the local reaction environment.

The electrochemical production of H_2O_2 is more favourable in alkaline conditions, particularly with carbon-based catalysts that promote the two-electron ORR pathway. In acidic media, H_2O_2 is thermodynamically less stable and undergoes rapid decomposition, posing significant challenges for its efficient and selective generation.[51,52]

This pH-dependence extends to the oxygen evolution reaction (OER). OER is the opposite reaction to the ORR; OER occurs on the anode side of regenerative fuel cells and rechargeable metal–air batteries when electricity is used either for recharging (in metal–air batteries) or producing oxygen from water (in regenerative fuel cells). This is also a multistep process that includes a series of intermediate species a nd requires a suitable catalyst for improving its kinetics, such as for the ORR. In acidic electrolytes, efficient and stable OER catalysis requires the use of noble metal oxides such as IrO_2 and RuO_2, due to the severe oxidative conditions and the limited activity of non-noble materials.[53,54] In alkaline media, however, earth-abundant transition metal oxides, such as those based on Ni, Co, or Fe, exhibit markedly improved OER kinetics and are widely employed as cost-effective alternatives.[53,55]

Beyond pH, the chemical composition of the electrolyte itself plays a critical role in modulating catalytic activity and reaction selectivity. Larger alkali metal cations, such as potassium (K^+) and cesium (Cs^+), influence the structure of the electric double layer, thereby affecting the adsorption and desorption dynamics of reactive intermediates at the electrode surface.[56,57] Specific anions, including phosphate (PO_4^{3-}) and carbonate (CO_3^{2-}) ions, may adsorb competitively on the catalyst's surface, leading to partial site blockage and suppression of catalytic activity. Buffering agents, such as phosphate buffers at neutral pH, help to stabilise the local pH near the electrode, which is particularly important under high current density conditions where substantial proton or hydroxide concentration gradients may develop.[57,58]

Morawa Eblagon and co-workers investigated the combined effects of the functionalisation temperature and the type and concentration of oxygen and nitrogen functionalities in a relatively similar class of materials, carbon xerogels (CXG).[59] They synthesised a series of CXG doped with nitrogen and determined that the onset potential and the number of electrons transferred during ORR in alkaline medium (0.1 M KOH) are highly dependent on the ratio of quaternary and pyrrolic nitrogen functionalities. The increase in functionalisation temperature from 650 °C to 950 °C resulted in a shift of the onset potential to more positive values, with the best activity displayed by N-CX functionalised at 950 °C (onset potential of 0.84 V *vs.* reversible hydrogen electrode (RHE)). This material also delivered the highest diffusion-limited current density of -4.8 mA cm^{-2}, with the number of exchanged electrons calculated to be 3.8, indicating an almost pure four-electron reduction.[59] It was also determined that particle size strongly impacts the electrochemical properties of the CXG catalyst. Reducing the particle size increased electrical conductivity and led to the introduction of carboxylic acid (–COOH) groups as active oxygen functional groups for the ORR.

Alvarez-Manuel *et al.* decorated nitrogen-doped carbon xerogel with Fe to obtain the highly active Fe–N–CXG material, which was investigated in 0.5 M H_2SO_4 towards the ORR.[60] To optimise Fe–N–CXG material synthesis *via* one-step urea polymerisation with resorcinol and formaldehyde, the authors systematically varied the urea : resorcinol ratio (U/R); this strongly influences the pore structure of the final product and, consequently, the number of active sites and mass transfer. Their results demonstrated that a U/R ratio 1 resulted in the most favourable pore formation, structure, and size distribution. The synthesised materials displayed an exchange of electrons close to 4, indicating the complete reduction of molecular oxygen to H_2O. The observed increase in activity can be attributed to several factors, including the mentioned optimal U/R ratio, efficient Fe incorporation into the carbon matrix, and a high concentration of pyridinic nitrogen, which resulted in a minimised pyrrolic/pyridinic nitrogen ratio.[60] It is worth mentioning that the increase in activity, as evidenced by a decrease in ORR overpotential, is observed with consecutive thermal treatment of the synthesised materials. However, although overpotential decreases, the consecutive thermal treatment also led to a decrease in diffusion-limited current density, suggesting the existence of an optimal number of treatments to maximise the catalyst activity.[60] Furthermore, the catalyst's large porosity negatively affects its durability, rendering it more prone to corrosion. This highlights the necessity of meticulously fine-tuning the synthesis process for each catalyst.

Carbon aerogels can be facilitated through both physical and chemical activation, facilitating the formation of micropores within the carbon matrix, leading to increased active sites and enhanced catalytic activity.[61] Experiments were conducted involving physical activation techniques (utilising CO_2 and

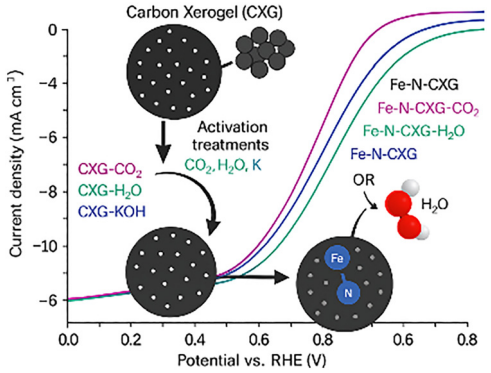

Fig. 3 Activated carbon xerogels enhance Fe–N–C catalysts and their performance by increasing microporosity, enabling higher Fe/N uptake and improved ORR activity.[61]

steam) and chemical activation with KOH. The findings demonstrated that materials subjected to physical activation exhibited superior catalytic performance (Fig. 3). Namely, Fe–N–CXG–H_2O (the CXG activated with water steam) showed the best results in terms of the most positive onset and half-wave potential, low Tafel slope, and high number of exchanged electrons among a series of Fe–N–CXG. The number of exchanged electrons during the ORR of 4.0 suggested a four-electron mechanism, with a Tafel slope of 51 mV dec^{-1}, lower than that of commercial Pt/C, suggesting fast reaction kinetics.[61,62] Further considerations revealed that the physical activation of CXG led to a milder increase in surface area and pore volume. In contrast, the incorporation of nitrogen in the most active forms (pyridinic N and N bonded to metal) has the most decisive influence on the increase in ORR activity. On the other hand, while chemical activation led to a substantial increase in micropore volume, the attachment of N and Fe to the surface was significantly hindered by the altered surface chemistry, resulting in a decrease in ORR activity. When Fe–N–CXG–H_2O was tested in a fully assembled fuel cell, a reduction in activity was observed due to the increased hydrophilicity of the material resulting from the activation process. These results again highlight the limitations of solely relying on rotating disk electrode (RDE) experiments for evaluating newly synthesised materials. RDE experiments can provide information on the intrinsic activity of the catalyst in a controlled environment with oxygen dissolved in the aqueous electrolyte. In contrast, testing within a fully assembled fuel cell, where gaseous oxygen was used on an air cathode, provides a more realistic assessment of their performance.

Another method for potentially increasing the activity of carbon aerogel-based materials is the synthesis of aerogels in the form of a well-organised 3D structure. Shen and co-workers used biomass cellulose nanofibers (CNF), high N-content aramid nanofibers (ANF), and 2D graphene oxide to synthesise a 3D honeycomb aerogel with interconnected porous nanosheets *via* the specific directional freeze-casting method.[63] The synthesised support (CAGO) was then loaded with cadmium (Cd) to obtain Cd@CAGO, followed by the addition of ferrocene and a thermal treatment at 800 °C. Precursors such as GO and CNF were used because they possess a large number of oxygen functional groups, which can serve as a good source of multifunctional aerogel matrices. In contrast, negatively charged groups can influence the adsorption of metals. ANF was employed as the nitrogen precursor, and Cd was used to prevent the loss of active sites due to high-temperature pyrolysis and to increase the specific surface area of the material. The synthesised porous N-doped carbon aerogel anchored with a single atomic Fe site (Fe-SA@PNC) was tested as the ORR catalyst in 0.1 M KOH. The obtained results showed very high activity of Fe-SA@PNC, surpassing that of the commercial 20 wt% Pt/C catalyst. At 1600 rpm, the material reached a diffusion-limited current density of *ca.* −5.5 mA cm^{-2}, nearly identical to the tested Pt/C catalyst. The number of exchanged electrons was calculated to be 4.0, indicating a direct O_2 reduction mechanism, with a low Tafel slope value of 77 mV dec^{-1}, similar to that of Pt/C (78 mV dec^{-1}).[63] The observed high ORR performance of Fe-SA@PNC can be attributed to several key factors. Firstly, the presence of a hierarchical pore structure within the material significantly enhances the electrochemically active surface area. Secondly, the stable honeycomb morphology, coupled with the atomically dispersed Fe–N_4 active sites within the carbon support, contributes considerably to the observed activity. Fe-SA@PNC was further validated as an ORR catalyst through successful demonstration in a fully assembled Zn–air battery (ZAB).

Adding a second metal to decorate carbon aerogel materials can also boost their activity. For example, Li *et al.* have synthesised and tested Fe–Ni alloy nanoclusters (Fe–Ni ANCs) anchored on the N, S co-doped carbon aerogel (Fe–Ni ANC@NSCA) as an electrocatalyst for ORR in Zn–air batteries.[64] The material was synthesised *via* the freeze-drying of aniline hydrogel in the presence of tannic acid (TA), Fe^{3+}, and Ni^{2+} ions. They concluded that the optimal ratio of TA : Fe : Ni is 1 : 2 : 5, leading to the formation of quasi-2D porous nanosheets and high-density Fe–Ni alloy nanoclusters (Fig. 4). Scanning electron microscopy (SEM) showed a 3D macroporous structure composed of loosely quasi-2D carbon sheets, which can promote the diffusion of the electrolyte into the material to the N_4–Fe–O–Ni–N_4 active sites on which ORR takes place, contrary to the mono-metal decorated material where Fe–N_4 are the main active sites. Electrochemical investigations revealed that the ORR proceeds *via* a four-electron mechanism, indicating the direct and complete reduction of O_2. Furthermore, the material showed a half-wave potential of 0.876 V *vs.* RHE and a Tafel slope of 63 mV dec^{-1}.[64] Besides ORR, authors have tested the activity of Fe–Ni ANC@NSCA in the oxygen evolution potential region, concluding that the material exhibits promising bifunctional performance. A good OER activity of Fe–Ni ANC@NSCA, reflected in the high achieved current density, low Tafel slope (75 mV dec^{-1}), low overpotential to reach 10 mA cm^{-2} (260 mV), and good stability, indicates a high potential for application in OER catalysis.[64] Furthermore, a low ΔE value of 0.599 V, as one of the main parameters for comparing bifunctional performance, calculated as $E_{10\,mA\,cm^{-2},OER} - E_{1/2,ORR}$, suggests a good bifunctional potential of this carbon aerogel-based material.

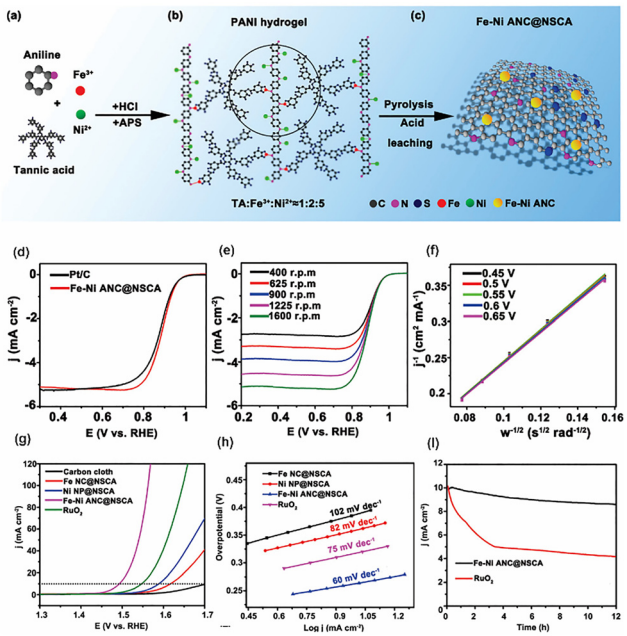

Fig. 4 (a)–(c) Steps of Fe–Ni ANC@NSCA synthesis. (d) LSV curves of Fe–Ni ANC@NSCA catalysts and commercial Pt/C catalysts on the RDEs, (e) LSV curves of Fe–Ni ANC@NSCA at various rotating speeds, (f) Koutecký–Levich plots of the Fe–Ni ANC@NSCA, (g) OER polarisation curves of carbon cloth, Fe NC@NSCA, Ni NP@NSCA, Fe–Ni ANC@NSCA, and commercial RuO_2, (h) Tafel plots of Fe NC@NSCA, Ni NP@NSCA, Fe–Ni ANC@NSCA, and commercial RuO_2, and (i) chronoamperometric curves of Fe–Ni ANC@NSCA and commercial RuO_2 for 12 h to evaluate their durability. Reproduced from ref. 64 with permission from Wiley, copyright 2025.[64]

Utilising a suitable template during the synthesis process offers a powerful means of controlling the structure and morphology of carbon aerogels, ultimately shaping the final catalyst architecture. For example, NaCl, one of the most common materials with a face-centred cubic (fcc) lattice, was used as a template for the synthesis of ultrathin carbon aerogels consisting of a few-layer graphene, GA_x (x represents the concentration of NaCl).[65] After the GA synthesis, NiFe-LDH (layered double hydroxide) colloids were adsorbed onto the GA, forming $(NiFe\text{-}LDH)_n/GA_x$, with $n = 1$, 2, and 3 signifying the loading of NiFe-LDH colloids. Testing in alkaline media revealed the best ORR activity of $GA_{0.18}$ with the most positive value of half-wave potential, 0.84 V *vs.* RHE, and n value of 3.87, suggesting a dominant four-electron pathway. On the other hand, when authors tested OER activity, better results were achieved with the materials containing NiFe-LDH colloids. Namely, the nanocomposite $(NiFe\text{-}LDH)_1/GA_{0.18}$ (NiFe-LDH 14.5 wt%) showed an overpotential to reach 10 mA cm^{-2} of 223 mV compared to 470 mV required by $GA_{0.18}$. These results indicated that the OER intrinsic activity arose primarily from the NiFe-LDH, with a minimal contribution from GA alone; however, the synergistic effect between GA and NiFe-LDH facilitated it. Therefore, the deposition of NiFe-LDH onto the GA matrix led to the synthesis of a material that was active for both ORR and OER, making it a potential bifunctional electrocatalyst for regenerative fuel cell and air-battery applications. The ΔE value was determined to be 0.61 V, lower than that exhibited by the Pt/C-RuO_2 catalyst employed as a benchmark in this study.[65]

It is worth noting that electrocatalysts based on carbon aerogels and xerogels often outperform commercial catalysts in terms of activity, durability, and long-term stability. Long-term stability is typically probed by chronoamperometric measurements at a constant potential, chronopotentiometry measurements at a given current density, or continuous cycling.[66,67] Physicochemical characterisation after the stability tests further confirms that the aerogel structure, morphology, and composition are preserved. In the case of aerogels with metal nanoparticles, the aerogels' porous microstructure, *i.e.*, an interconnected skeleton, prevents Ostwald ripening and aggregation of the nanoparticles. This was confirmed, for example, in the case of N-doped "dual-network" carbon aerogels (FeCo/N-DNC).[68] Chronoamperometric measurements under ORR/OER conditions for 10 000 s demonstrated a current loss of only 19.7% for FeCo/N-DNC (in comparison with >35.0% loss for the commercial Pt/C). Good long-term stability was attributed to (i) the confined particles within a 3D interconnected framework being stabilized, (ii) the 3D porous structure preventing metal particles agglomeration and dissolution, and (iii) the outer layer of carbon preventing direct contact of the metal particles with harsh environments. Furthermore, when used as the air-cathode in a rechargeable Zn–air battery, FeCo/N-DNC aerogel maintained a network structure with a homogeneous distribution of FeCo particles upon cycling, corroborating the aerogel's structural stability. FeCo metal content in FeCo/N-DNC aerogel increased for >3 wt% (25.7 wt% *vs.* 22.8 wt%), most likely due to partial carbon corrosion under the harsh battery conditions.[68]

Carbon aerogel with honeycomb-like structure, double-doped with N and S and loaded with FeCo alloy nanoparticles (NSCA/FeCo) demonstrated excellent durability during continuous cycling (8000 cycles) under ORR conditions as evidenced by a stable diffusion-limiting current density and a negative shift of the half-wave potential by only 15 mV (in contrast, commercial Pt/C showed a notably higher shift of 96 mV).[69] Somewhat lower durability under OER conditions was observed, with the overpotential at 10 mA cm^{-2} increasing by 50 mV (slightly higher than the 33 mV increase observed for RuO_2); the increase was attributed to the carbon network erosion and partial oxidation of exposed alloy particles. A liquid flow ZAB with NSCA/FeCo as air-cathode maintained a low charge–discharge voltage gap of ~0.82 V and sustained a round-trip efficiency of 58% after 250 cycles, outperforming Pt/C + RuO_2, which showed significant performance degradation after only 20 cycles. Moreover, a flexible ZAB with NSCA/FeCo as an air cathode demonstrated a decrease in the round-trip efficiency at 1 mA cm^{-2} of only 6% (61.3% to 55.3%) after 450 consecutive charge–discharge cycles. In contrast, the mixed commercial catalyst battery showed a sharp increase in the voltage gap after just 83 cycles.[69]

In this section, we have provided a preliminary overview of the broad potential of carbon aerogel-based materials as

catalysts for ORR and OER and strategies for further enhancing their performance. This offers a strong foundation for the development of highly efficient and versatile electrocatalysts for energy storage and conversion applications. Experimental evidence demonstrates their ability to efficiently catalyse ORR through the preferred four-electron pathway and their potential for OER activity when integrated with appropriate active metals and sites, suggesting promising bifunctional catalytic performance.

3.2. Carbon aerogels as electronic materials for supercapacitors

Electrochemical capacitors, a distinct class of electrochemical devices for energy storage and conversion, may differ in their charge storage mechanisms. In electric double-layer capacitors (EDLCs), charge storage occurs through the reversible adsorption of electrolyte ions onto the surface of the active material, without involving any oxidation–reduction processes.[70–72] In contrast, pseudocapacitors (PS) store charge through fast and reversible charge-transfer processes occurring at the electrode surface. Specifically, the charge accumulation mechanism involves reversible oxidation–reduction reactions between electrolyte ions and the active surface functional groups of the electrode material.[73,74] A third category is represented by hybrid capacitors, whose operation is based on a combination of EDLC and pseudocapacitive mechanisms, resulting in a synergistic contribution to the device's overall capacitance. This mechanism is observed for electrode materials combining carbon materials with metal sulphides or oxides. The contributions of each mechanism can be quantitatively distinguished by the so-called Dunn's analysis starting from eqn (8):[75]

$$i(\nu) = k_1\nu + k_2\nu^{1/2} \quad (8)$$

where i is the current at a given scan rate ν, k_1 is the constant associated with the EDL contribution, and k_2 is the constant associated with the faradaic (pseudocapacitive) contribution. Carbon aerogels have gained popularity as electrode materials for supercapacitors in recent years due to their exceptional stability and high specific capacitance. However, further improving their specific capacitance remains a challenging goal. A promising approach to achieving this is to combine them with metals, metal oxides, or to dope them with nitrogen. Therefore, He and co-workers synthesised several catalysts to investigate the individual effects of Co and Ni sulphides aerogels with S and N-co-doped graphene aerogel (SNGA), Ni-S/SNGA, Co-S/SNGA, as well as their synergistic effect by altering the ratio between Co and Ni in $CoNi_2S_4$/SNGA and $NiCo_2S_4$/SNGA (Fig. 5). Additionally, SNGA played a key role in enhancing stability and improving capacity compared to ordinary graphene. Specifically, the samples were synthesised *via* a hydrothermal method using appropriate precursors of Co and Ni with sulphides to examine their synergistic effect, as well as from Ni or Co in sulphide form. These forms were introduced into dispersed graphene that had been previously doped with nitrogen and subjected to a sintering process to obtain a stable

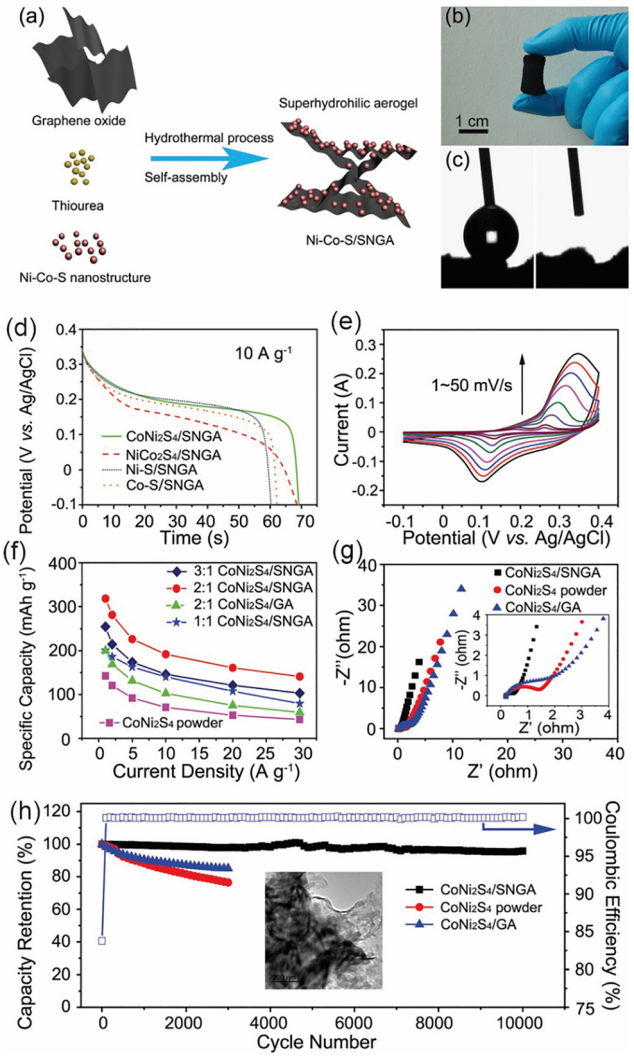

Fig. 5 (a) Schematic illustration of the $NiCo_2S_4$/SNGA synthesis process; (b) digital photograph of the resulting aerogel; (c) contact angle images before (left) and after (right) water droplet application. (d) Discharge curves of $CoNi_2S_4$/SNGA, $NiCo_2S_4$/SNGA, NiS/SNGA, and Co-S/SNGA at the current density of 10 A g^{-1}; (e) cyclic voltammetry curves of $CoNi_2S_4$/SNGA at the scan rate of 1–50 mV s^{-1}; (f) the comparison of specific discharge capacity for different ratios of $CoNi_2S_4$/SNGA, $CoNi_2S_4$/GA, and $CoNi_2S_4$ powder samples as a function of current densities; (g) Nyquist curves of $CoNi_2S_4$/SNGA, $CoNi_2S_4$/GA, and $CoNi_2S_4$ electrodes, inset showing high-frequency parts of the EIS spectra for these samples; (h) cycling performance of the $CoNi_2S_4$/SNGA for 10 000 cycles and $CoNi_2S_4$/GA and $CoNi_2S_4$ electrodes for 3000 cycles, respectively, inset showing the TEM image of the $CoNi_2S_4$/SNGA after long-term cycling.[76]

nanostructured aerogel.[76] Metal sulphides are also commonly used in energy storage due to their redox centres and active sites.[76] SEM analysis revealed that $CoNi_2S_4$/SNGA and $NiCo_2S_4$/SNGA samples had better-developed pores and evenly distributed Ni–Co–S nanoparticles than the Ni–S/SNGA and Co-S/SNGA samples. It is also observed that the Ni particles in the sulphide Ni–S form were smaller and sporadically distributed on the graphene, as were the Co particles in the Co–S form, which formed in somewhat larger groups.[76]

The electrochemical properties of the synthesised samples were investigated using cyclic voltammetry (CV) and galvanostatic charge–discharge (GCD) in a 6 M KOH electrolyte.[76] At a current density of 10 A g^{-1}, the specific capacity values of $CoNi_2S_4$/SNGA, $NiCo_2S_4$/SNGA, Ni–S/SNGA, and Co–S/SNGA were 192.1, 190.9, 167.5, and 184.0 mAh g^{-1}, respectively (Fig. 5). These samples maintained about 44% of their original capacity when the current density increased 30 times. The $CoNi_2S_4$/SNGA showed the best performance, attributed to the rich redox centres and the synergistic effect of Ni and Co ions. Analysis of the voltammetric curves revealed distinct redox peaks, indicating that the processes were governed by semi-infinite diffusion, which suggests that the materials operate through reversible faradaic reactions (Ni^{2+}/Ni^{3+} and $Co^{2+}/Co^{3+}/Co^{4+}$).[76] GCD tests further confirmed the suitability of these materials for electrochemical energy storage devices. $CoNi_2S_4$/SNGA exhibited a high specific capacity of 318.3 mAh g^{-1} at 1 A g^{-1}, with good rate capability (44.3% retention at 30 times higher current density). The material's superior performance was attributed to the optimal ratio of nanoparticles and SNGA, as well as its efficient charge storage properties. Additionally, EIS showed that $CoNi_2S_4$/SNGA had the smallest charge-transfer resistance (R_{ct} = 0.43 Ω), indicating the material's high electronic conductivity and efficient charge storage compared to other samples.[76]

In another study, carbon nanofiber aerogels (CNF) were prepared using polyacrylonitrile (PAN) and polyvinylpyrrolidone (PVP) in different ratios (0, 0.5, 1, and 2) as precursors, followed by hydrogelation and freeze-drying. Afterwards, the pre-oxidised aerogels were carbonised at various temperatures (700, 800, 900, and 1000 °C) to achieve the desired structure and properties (Fig. 6a).[77] The CNF-1-900 aerogel exhibited the best electrochemical performance in terms of specific capacity, high current rate capability, and stability during cycling. It showed an outstanding specific capacity of 285 F g^{-1} at a current density of 1 A g^{-1}. It retained 80% of its initial capacity after 10 000 cycles in 3 M KOH.[77] The good electrochemical performance of this sample was attributed to its high graphitisation and large surface area, which enabled more efficient charge storage and faster charge/discharge kinetics. To improve the surface activity and energy storage capacity, Zhang and co-workers further activated CNF-1-900 aerogel with CO_2 for different durations (5, 30, and 45 min).[77] This activation process aimed to further increase the material's surface area and optimise its electrochemical properties for better performance in supercapacitor applications.

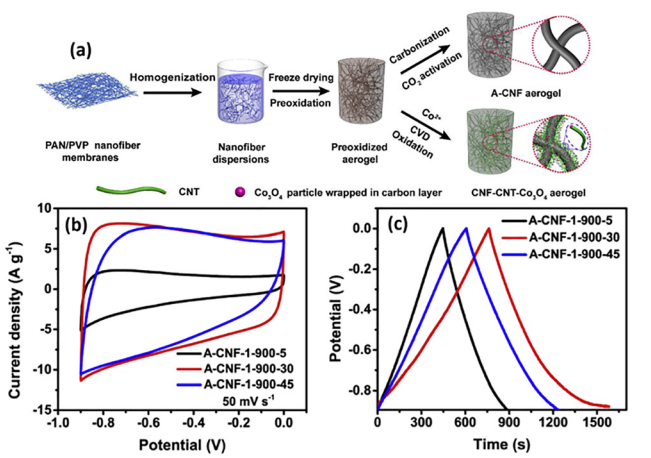

Fig. 6 (a) Schematic illustrating the syntheses of A-CNF aerogel anode material and CNF-CNT-Co_3O_4 aerogel cathode material; (b) CV curves, and (c) GCD curves for A-CNF-1-900-5, A-CNF-1-900-30 and A-CNF-1-900-45 samples. Reproduced from ref. 77 with permission from Elsevier, copyright 2025.

The analysis of CV curves of these aerogels (Fig. 6b) shows that the aerogel activated for 5 min (A-CNF-1-900-5) displayed a minor increase in surface area and specific capacitance. At the same time, the 30-minute activation (A-CNF-1-900-30) led to a significant enhancement in both specific capacitance and rate performance at higher current densities. The increase in surface area and mesopore development during the 30-minute activation notably improved the ion diffusion and charge-storage efficiency, which was reflected in the corresponding GCD curves (Fig. 6c). The maximum specific capacitance of the A-CNF-1-900-30 reached 300 F g^{-1} at 0.3 A g^{-1}, showing 1.3 times increase. Moreover, it retained good performance at high current densities.[77] On the other hand, the 45-minute activation (A-CNF-1-900-45) showed further improvements in surface area but with diminishing returns. Despite an increase in surface area, excessive activation led to structural changes, resulting in reduced stability and no significant improvement in electrochemical performance. This suggests that longer activation times can compromise the material's structural integrity. Furthermore, the A-CNF-1-900-30 electrode exhibited lower charge-transfer resistance. Notably, it also showed outstanding cycling stability, maintaining 93.3% of its capacitance after 10 000 cycles at 5 A g^{-1}.[77] This performance highlights that the 30 min CO_2 activation was the most effective for optimising the electrochemical properties of the A-CNF-1-900 aerogel, improving both its energy storage capacity and rate performance.

To preserve the environment while reducing production costs, there is a focus on utilising waste materials from biomass for the preparation of novel materials. Phong *et al.* used Ni-doped carbon aerogel derived from nipa palm shell (Ni-NS-CA) to fabricate supercapacitor electrodes. The green synthesis of the mentioned material consists of three processes: hydrogel formation through crosslinking (SA, Ni^{2+}), freeze-drying, and pyrolysis.[78] It should be noted that Ni^{2+} is doped into CA using sodium alginate as a crosslinking agent to enhance electron mobility. Ni is a highly conductive transition metal that can easily change oxidation states, making it an effective catalyst in various electrochemical reactions.

Electrochemical measurements were performed in a three-electrode system using 1 M Na_2SO_4 as the electrolyte, with CV, GCD, and EIS measurements employed.[78] Ni-NS-CA was tested at 10, 15, and 100 mV s^{-1}; the specific capacitance was 10.1, 38.91, and 26.07 F g^{-1}, respectively. Additionally, from Fig. 6b, it can be seen that the curves are nearly rectangular without noticeable oxidation or reduction peaks. This can be attributed to

the relatively small amount of Ni, which indicates a minor involvement in redox reactions in the neutral electrolyte. Additionally, the relatively low resistance of 320 Ω obtained from the Nyquist plot suggests that Ni-NS-CA exhibits a good energy storage capacity. In addition to specific capacitance, specific energy and specific power were also calculated. As the scan rate increases (10, 15, 100 mV s^{-1}), the specific energy decreases in the order 14.5 Wh kg^{-1} < 5.41 Wh kg^{-1} < 3.62 Wh kg^{-1}, while the specific power increases from 260.4 W kg^{-1}, over 486.4 W kg^{-1} to 651.8 W kg^{-1}, respectively. The increase in specific power with the increasing scan rate indicates that a larger number of electrons can be loaded, which affects the kinetics and mass transport processes, thereby increasing the current.[78] The GCD curves demonstrate the system's stability. Each charge and discharge cycle of the Ni-NS-CA sample lasted approximately 2s, indicating a relatively fast charging capability. Also, during the 4 cycles shown (Fig. 6c), there were no significant changes in the shape of the GCD curve, demonstrating the ability to maintain stable charging/discharging performance.[78]

Lee and coworkers prepared carbon aerogel by the polycondensation of resorcinol and formaldehyde, using Na_2CO_3 as a catalyst, with a resorcinol-to-catalyst ratio of 500. Co-doped carbon aerogels were then prepared by an impregnation method with varying cobalt content (1, 3, 7, 10, and 15 wt%), and their performance as supercapacitor electrodes was investigated by measuring specific capacitance in 1 M H_2SO_4 electrolyte at a scan rate of 10 mV s^{-1}.[79] Among the prepared samples, the 7 wt% Co-doped carbon aerogel exhibited the highest capacitance of 100 F g^{-1}, which was attributed to the faradaic redox reactions of cobalt oxide. The specific capacitance values were 72, 77, 80, 86, and 87 F g^{-1}, increasing in the order 15, 1, 3, 10, and 5 wt% of Co, respectively.[79] Since the 7 wt% Co-doped carbon aerogel showed the best performance, 7 wt% Cu-, Fe-, Mn-, and Zn-doped carbon aerogels were also prepared. Among the transition metal-doped carbon aerogels, the Mn-doped carbon aerogel exhibited the highest capacitance of 107 F g^{-1}, somewhat higher than the Co-doped aerogel. The capacitance values for the other metals were 94, 91, 88, and 81 F g^{-1} for Cu-, Fe-, Zn-, and carbon aerogels, respectively.[79]

On the other hand, Cu- and Fe-doped carbon aerogels exhibited the most stable cyclability. To investigate the stability of transition metal (Co, Cu, Fe, Mn, Zn)-doped carbon aerogels, CVs were recorded over 30 cycles. Symmetrical peaks that originate from the faradaic reactions could be observed. However, only Cu- and Fe-doped carbon aerogels demonstrated stable cyclability, indicating the long-term electrochemical stability of these materials, while Mn-doped carbon aerogels suffered significant degradation. This is attributed to the cathodic dissolution of MnO_2 during the cathodic potential sweep in the acidic medium (Table 1).[79]

4. Applications in environmental solutions

Hydrogen peroxide is one of the most essential chemicals in the world, widely used in various industries, laboratories, and households. This compound is a strong oxidising agent, but it is environmentally acceptable, which is why it is extensively used for synthesising polymers and pharmaceutical products, bleaching cellulose, paper, and textiles, as well as treating wastewater and ballast water.[82] Also, it is often used to disinfect various surfaces in households and industry, especially in the wine industry, to clean the outer parts of barrels. It is predicted that the global H_2O_2 market will grow to USD 7.07 billion this year, while in the next decade (by 2034), it will reach a value of about USD 11.54 billion, which will represent a CAGR (compound annual growth rate) of 5.6% between 2024 and 2034.[83]

Currently, 95% of industrial H_2O_2 production occurs *via* the anthraquinone autoxidation (AO) process. In this process, 2-alkyl-anthroquinone (AQ) is hydrogenated in an organic solvent over a Pd catalyst and then oxidised with O_2 to produce H_2O_2, allowing for the recovery of AQ. The process is completed by extracting H_2O_2 and treating the working solution for reuse.[84,85] Although an extremely high yield of H_2O_2 (99%) is obtained, the key disadvantages of this multi-step production method are the high price of the Pd-based catalyst, high level of contamination with organic waste, the use of complex and extensive infrastructure and energy-intensive distillation steps. This process produces a large amount of concentrated H_2O_2, which means that transporting, storing, and handling bulk H_2O_2 pose certain safety risks and incur high costs.[86–88]

Consequently, the latest research aims to find alternative methods of producing H_2O_2. Among all the recently developed technologies in this field, the electrochemical selective two-electron oxygen reduction reaction stands out as a promising candidate.[87–89] It enables the continuous production of diluted H_2O_2, thereby eliminating the disadvantages of the conventional process.

The electro-Fenton process is one of the most important technological procedures in wastewater treatment. During this process, H_2O_2 can be continuously electrogenerated *in situ* through the selective $2e^-$ ORR pathway, thus avoiding environmental pollution, transport, and storage of excess H_2O_2 and facilitating operation under mild conditions. During this process, catalytic production of H_2O_2 in the presence of Fe(II) ions as Fenton catalysts leads, upon reduction of H_2O_2 by Fe^{II}, to the formation of hydroxyl radicals ($OH^{\bullet}$) (eqn (9)), which have a high oxidation potential (2.80 V) and a high electronic affinity (569.3 kJ mol^{-1}).[80] The large surface area and customisable porosity make carbon aerogels effective for electro-Fenton processes and wastewater treatment.

$$Fe^{II} + H_2O_2 \rightarrow Fe^{III} + OH^- + OH^{\bullet} \quad (9)$$

For example, Tian *et al.* investigated and compared the electrocatalytic activity of Fe–carbon aerogel with sulphur (FeSCA) and without sulphur (FeCA) towards H_2O_2 electrogeneration.[80] Introducing Fe into the carbon-based electrode typically favours the $4e^-$ ORR pathway and limits the $2e^-$ ORR pathway. Rotating ring-disc electrode (RRDE) measurements revealed that both disc current I_d and ring current I_r and their ratio, I_d/I_r, are higher for FeSCA than FeCA, indicating a higher

Table 1 Comparison of carbon and graphite aerogels' performance in electrochemical energy conversion and storage devices

Material	S_{BET} [m^2 g^{-1}]	Pore size [μm]	V_{tot} [cm^3 g^{-1}]	Electrolyte	E_{onset} [V]	$E_{1/2}$ [V]	b [mV dec^{-1}]	n	Ref.
Fe-N-CXG-H_2O	na	na	na	0.5 M H_2SO_4	0.78	0.65	51	4.0	61
FeSCA-900	1060	2–4	na	0.1 M $HClO_4$	0.306	na	na	2	80
FeCA-900	512	2–4	na	0.1 M $HClO_4$	0.442	na	na	4.0	80
Ni-NS-CA	83.873	2.12 nm	na	1 M Na_2SO_4	na	na	na	na	78
FeNi-CA	589.0	20 nm	0.155	0.1 M Na_2SO_4	0.421	na	na	2.5–2.7	81
Fe-CA	609.7	25 nm	0.162	0.1 M Na_2SO_4	0.442	na	na	4.0	81
Ni-CA	665.9	8.6 nm	0.138	0.1 M Na_2SO_4	0.866	na	na	4.0	81
$GA_{0.18}$	328.1	<1	na	0.1 M PBS	na	0.701	77	3.89	65
$GA_{0.18}$	328.1	<1	—	0.1 M KOH	0.976	0.84	79	3.87	65
$(NiFe\text{-}LDH)_1/GA_{0.18}$ (NiFe-LDH 14.5 wt%)	na	na	na	0.1 M PBS	na	0.738	na	na	65
$(NiFe\text{-}LDH)_1/GA_{0.18}$ (NiFe-LDH 14.5 wt%)	na	na	na	0.1 M KOH	na	na	78	na	65
CX_NH3_950_BM (N-CX)	1048	25	1.8	0.1 M KOH	0.84	na	na	3.8	59
Fe-SA@PNC	1036.7	20–50		0.1 M KOH	0.98	0.87	77	4.0	63
Fe–Ni ANC@NSCA	241.2	na	0.24	0.1 M KOH	na	0.891	63	na	64
$CoNi_2S_4$/SNGA	na	na	na	0.1 M KOH	na	na	na	na	76
$NiCo_2S_4$/SNGA	na	na	na	0.1 M KOH	na	na	na	na	76
Ni-S/SNGA	na	na	na	0.1 M KOH	na	na	na	na	76
Co-S/SNGA	na	na	na	0.1 M KOH	1	na	na	3.8–3.95	76
CNF-1-900 aerogel	na	na	na	3 M KOH	na	na	na	na	77
A-CNF-1-900-30	na	na	na	3 M KOH	na	na	na	na	77

Use for supercapacitors

Material	Electrolyte	C_S/mAh g^{-1}	Sp. capacitance [F g^{-1}]	Ref.
Fe–Ni ANC@NSCA	0.1 M KOH	750.7 at 10 A g^{-1}	na	64
$CoNi_2S_4$/SNGA	0.1 M KOH	192.1 at 10 A g^{-1} and 318.3 at 1 A g^{-1}	na	76
$NiCo_2S_4$/SNGA	0.1 M KOH	190.9 at 10 A g^{-1}	na	76
Ni-S/SNGA	na	167.5 at 10 A g^{-1}	na	76
Co-S/SNGA	na	184.0 at 10 A g^{-1}	na	76
CNF-1-900 aerogel	na	285 at 1 A g^{-1}	132	77
A-CNF-1-900-30	na	na	300	77
Ni-NS-CA	na	na	104.1	78

OER parameters

Material	b [mV dec^{-1}]	$\eta_{10\,mA\,cm^{-2}}$ [mV]	ΔE	Ref.
Fe–Ni ANC@NSCA	60	260	0.599	64
$GA_{0.18}$	283	470	na	65
$(NiFe\text{-}LDH)_1/GA_{0.18}$ (NiFe-LDH 14.5 wt%)	43	223	0.611	65

na* = data not available; S_{BET} = the specific surface area; V_{tot} = total voltage; E_{onset} = onset potential; $E_{1/2}$ = half-wave potential; b = Tafel slope; n = number of electrons transferred.

yield of H_2O_2. Moreover, FeSCA also had a more positive ORR onset potential at −0.152 V *vs.* SCE (*ca.* 0.306 V *vs.* RHE) in an acidic medium (0.1 M $HClO_4$). The selectivity of H_2O_2 generation by the $2e^-$ ORR at FeSCA increased by 200% compared to FeCA. These results indicate that the introduction of sulphur into the Fe–carbon matrix favours the formation of –COOH functional groups, facilitates the regeneration of Fe(II) on the surface of the electrocatalyst, and causes an improvement in the activity and selectivity of the H_2O_2 generation. Ultimately, this leads to improved efficiency of the contaminants' degradation by the heterogeneous electro-Fenton process and their more efficient removal in a relatively short time.[80]

Carbon aerogel modified with a Fe–Ni alloy (FeNi-CA) can be used as the cathode in an electro-Fenton process for the degradation of acetaminophen. The improvement of electrocatalytic performance for the H_2O_2 production compared to pure aerogel or single-metal modified aerogel is a consequence of the unique microstructure of FeNi-CA (in which alloy nanoparticles are present), carbon defects, and a large number of oxygen functional groups. FeNi-CA showed good electrocatalytic performance towards the $2e^-$ ORR in a wide pH range and at a low current density of about 4.44 mA cm^{-2}. Under suitable conditions, it is possible to remove almost the entire amount of acetaminophen. The use of FeNi-CA for *in situ* H_2O_2 generation eliminates the need for external aeration and chemical agents. An additional advantage of this material is its suitability for permanent use in an electro-Fenton process, where double functionality is achieved because oxygen reduction occurs at the cathode and oxygen evolution at the anode.[81]

Ye *et al.* investigated the activity and selectivity of the FeNi-CA, Fe-CA, and Ni-CA electrodes towards $2e^-$ ORR in neutral media, Fig. 7. FeNi-CA showed significantly improved H_2O_2 selectivity and production compared to pure CA due to the incorporation and synergistic effect of Fe and Ni in the CA matrix.[81] The onset potentials for FeNi-CA, Fe-CA, and Ni-CA were determined to be 0.421 V, 0.442 V, and 0.866 V *vs.* RHE, respectively. In the potential range from −0.4 V to 0.2 V *vs.* RHE, FeNi-CA demonstrated the highest H_2O_2 selectivity of 60–

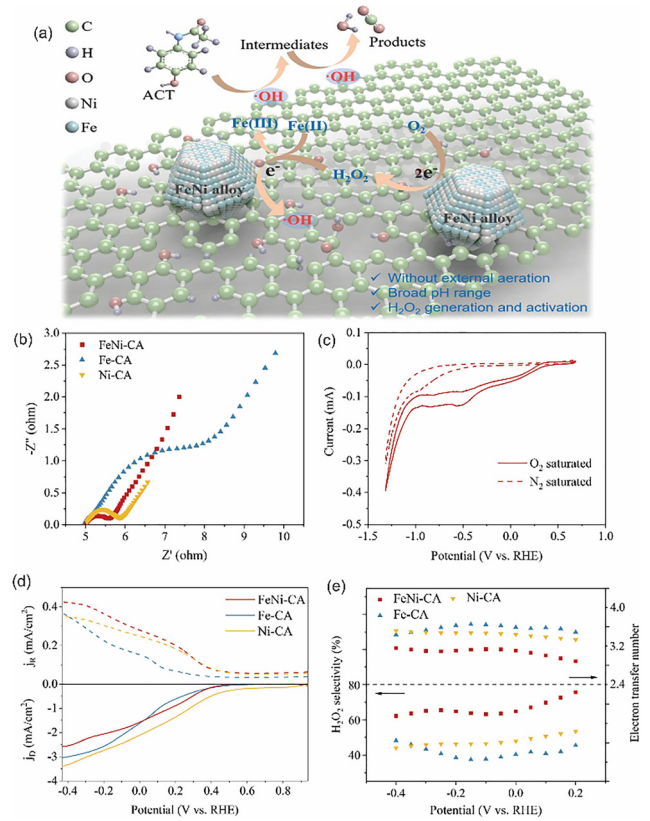

Fig. 7 (a) Schematic representation of two-electron ORR to H_2O_2 at FeNi-CA; (b) EIS Nyquist plots; (c) CV curves of FeNi-CA in O_2 and N_2 atmospheres; (d) polarization curves of FeNi-CA, Fe-CA and Ni-CA with simultaneous H_2O_2 oxidation currents at the ring electrode in 0.1 M Na_2SO_4 (pH = 3); (e) calculated electron transfer number and H_2O_2 selectivity.[81]

80%, higher than both monometallic Fe-CA and Ni-CA counterparts. The activity of FeNi-CA towards the $2e^-$ ORR process is confirmed by the number of exchanged electrons of 2.5–2.7. Conversely, the number for ORR at Fe-CA and Ni-CA was close to 4, indicating a complete $4e^-$ reduction of O_2 to H_2O.

CXs synthesised by the hydrothermal carbonisation of glucose and polyaniline (PANI) could also be used as catalysts for the electrochemical H_2O_2 production from O_2.[90] The performance towards H_2O_2 production can be easily adjusted by the polymerisation temperature of PANI (0–80 °C), where the reaction onset potential (−0.45 to −0.29 V) decreases, while the catalytic activity and H_2O_2 selectivity (47–94%) increase with the polymerisation temperature. Liang *et al.* have tested several different CXs (prepared at 0, 20, 40, 60, and 80 °C) and concluded that CX-80 shows the best catalytic activity with an excellent selectivity towards H_2O_2 of 94% in neutral media. The excellent electrocatalytic performance of CX-80 was attributed to its large volume of meso/macropores and high C═O content. In the potential range from 0.35 to 0.80 V, the electron transfer number values of 2.1 under neutral conditions indicate that the two-electron ORR takes place on CX-60 and CX-80. In the same potential range, the H_2O_2 selectivity of CX-80 reaches 85–94%, which is comparable to the values for the best two-electron ORR electrocatalysts such as Pt–Hg (92%) and Au (95%).

Most newly developed carbon-based electrocatalysts, such as those incorporating noble metals, exhibit high H_2O_2 selectivity, but only under acidic or basic conditions. However, CX-80 exhibits high selectivity even in a neutral environment, making it suitable for *in situ* H_2O_2 production and wastewater treatment *via* the electro-Fenton process.[90]

5. Conclusions and future perspective

This review has traversed the significant advancements in carbon aerogels and xerogels, highlighting their profound potential across energy storage, environmental remediation, and catalysis. Beyond merely summarizing their enhanced functional properties through strategies like metal- and nitrogen-doping or the incorporation of advanced precursors, a deeper understanding emerges regarding the critical design principles and evolutionary trends in these materials.

A key lesson learned is the importance of tailoring microstructural features and surface chemistry to dictate electrochemical performance. The literature consistently demonstrates that optimizing pore size distribution (integrating micro-, meso-, and macropores), controlling hierarchical porosity, and engineering particle size are not merely incremental improvements but fundamental determinants of charge transport, ion diffusion, and active site accessibility. Specifically, a judicious balance of high surface area from micropores for charge storage and efficient ion diffusion pathways from mesopores, complemented by macropores acting as ion-buffering reservoirs, is crucial for maximizing both energy and power densities. Similarly, particle size reduction generally enhances active sites and rate performance, though excessive reduction can lead to instability and agglomeration, emphasising the necessity of meticulous fine-tuning.

Furthermore, the review reveals a clear trend towards multifunctionality and synergistic effects in achieving superior performance. Simple doping strategies have evolved into sophisticated co-doping (*e.g.*, N, S co-doping) and hybrid material designs (*e.g.*, metal-decorated aerogels, bimetallic oxides). The evidence strongly suggests that the most impactful enhancements arise not from isolated modifications but from the synergistic interplay between different components, such as the combined effect of specific nitrogen functionalities (*e.g.*, pyridinic nitrogen for $4e^-$ ORR) and precisely incorporated metal active sites. This synergy is crucial for promoting desired reaction pathways, improving kinetics, and boosting overall catalytic activity, often outperforming commercial benchmarks.

The evolution of synthetic methodologies also highlights the importance of structure control at multiple scales. Techniques like directional freeze-casting to create well-organized 3D honeycomb aerogels or templates like NaCl to synthesize ultrathin graphene aerogels depict a shift towards precise architectural engineering beyond basic polymerization and carbonization.

These advanced synthetic approaches enable the creation of highly interconnected porous networks that enhance electrochemical performance and significantly improve the long-term stability and durability of the materials by preventing issues like nanoparticle aggregation and corrosion, particularly vital for practical applications in devices like Zn–air batteries.

Despite these advancements, challenges remain in optimising the synthesis processes, scaling up production, and further enhancing the performance of carbon aerogels for specific applications. Future research should focus on exploring novel precursors, improving the structural integrity of aerogels, and developing multifunctional materials that combine energy storage and catalytic properties. By addressing these challenges, carbon aerogels have the potential to revolutionise energy storage, environmental remediation, and catalysis, contributing to a more sustainable and energy-efficient future.

The overarching lesson for designing advanced carbon aerogel systems is to move beyond empirical trial-and-error towards a holistic design paradigm. This involves a deep understanding of how synthesis parameters, precursor selection (including sustainable alternatives), and post-synthesis treatments collectively influence the hierarchical pore structure, surface functionalization, and the dispersion of active sites. The key factors at play are precise control over doping types and concentrations, judicious selection of metal decorators, and the development of sophisticated 3D architectures that facilitate optimal mass transport and charge transfer, ultimately leading to enhanced efficiency and stability in demanding electrochemical applications. By integrating these insights, readers can be guided not just to enhance existing systems, but to innovatively design next-generation carbon aerogel-based materials with tailored properties for specific sustainable technologies.

Conflicts of interest

There are no conflicts to declare.

Data availability

No primary research results, software or code have been included, and no new data were generated or analysed as part of this review.

Acknowledgements

The authors would like to thank the Ministry of Science, Technological Development and Innovation of the Republic of Serbia (contract number: 451-03-136/2025-03/200146 and 451-03-137/2025-03/200146) as well as Fundação para a Ciência e a Tecnologia (FCT, Portugal) for funding a Principal Researcher contract (2023.09426.CEECIND, **https://doi.org/10.54499/2023.09426.CEECIND/CP2830/CT0021**) in the scope of the Individual Call to Scientific Employment Stimulus – 6th Edition (D.M.F.S), and for funding Centro de Quimica Estrutural through projects UIDB/00100/2020 (DOI: 10.54499/UIDB/00100/2020), UIDP/00100/2020 (DOI: 10.54499/UIDP/00100/2020), and LA/P/0056/2020 (DOI: 10.54499/LA/P/0056/2020).

Notes and references

1 W. Xu, N. Fu, Z. Chen, D. Li, Y. Liu and Z. Yan, *Case Stud. Chem. Environ. Eng.*, 2024, **9**, 100629.
2 K. A. A. A. Elsehsah, Z. A. Noorden and N. M. Saman, *J. Energy Storage*, 2024, **97**, 112788.
3 A. C. Pierre and G. M. Pajonk, *Chem. Rev.*, 2002, **102**, 4243–4265.
4 N. Ding, B. Liang, X. Gao, D. Yao, J. Chen, C. Liu, C. Lu and X. Pang, *Chem. Eng. J.*, 2024, **495**, 153470.
5 Y. Shen and J. Yang, *Green Chem.*, 2024, **26**, 8969–9004.
6 D. K. Sam, E. K. Sam, A. Durairaj, X. Lv, Z. Zhou and J. Liu, *Carbohydr. Res.*, 2020, **491**, 107986.
7 J. Song, X. Guo, J. Zhang, Y. Chen, C. Zhang, L. Luo, F. Wang and G. Wang, *J. Mater. Chem. A*, 2019, **7**, 6507–6513.
8 J. J. Feng, C. Zhang, J. J. Feng, Y. Jiang and N. Zhao, *ACS Appl. Mater. Interfaces*, 2011, **3**, 4796–4803.
9 A. Gutiérrez-Pardo, J. Ramírez-Rico, R. Cabezas-Rodríguez and J. Martínez-Fernández, *J. Power Sources*, 2015, **278**, 18–26.
10 J. H. Lee and S. J. Park, *Carbon*, 2020, **163**, 1–18.
11 Y. Hanzawa, H. Hatori, N. Yoshizawa and Y. Yamada, *Carbon*, 2002, **40**, 575–581.
12 R. W. Pekala, *J. Mater. Sci.*, 1989, **24**, 3221–3227.
13 M. Li, B. Pang, S. Dai, Y. Cui, Y. Wu, H. Li and B. Luo, *Chem. Eng. J.*, 2024, **499**, 156693.
14 X. Zhang, J. Zhou, Y. Zheng, H. Wei and Z. Su, *Chem. Eng. J.*, 2021, **420**, 129700.
15 L. Paliotta, G. De Bellis, A. Tamburrano, F. Marra, A. Rinaldi, S. K. Balijepalli, S. Kaciulis and M. S. Sarto, *Carbon*, 2015, **89**, 260–271.
16 D. Lv, T. Zhang, D. Wang, J. Li and L. Wang, *Ind. Crops Prod.*, 2021, **170**, 113750.
17 D. R. Rolison, M. B. Sassin and J. W. Long, *Springer Handbooks*, 2023, Part F1485, pp. 1305–1332.
18 J. Wang, H. Kong, J. Zhang, Y. Hao, Z. Shao and F. Ciucci, *Prog. Mater. Sci.*, 2021, **116**, 100717.
19 Y. Shi, Y. Xia, G. Xu, L. Wen, G. Gao and B. Zong, *Chin. J. Chem. Eng.*, 2022, **41**, 145–161.
20 S. Fan, J. Chen, C. Fan, G. Chen, S. Liu, H. Zhou, R. Liu, Y. Zhang, H. Hu, Z. Huang, Y. Qin and J. Liang, *J. Hazard. Mater.*, 2021, **416**, 126225.
21 S. Araby, A. Qiu, R. Wang, Z. Zhao, C. H. Wang and J. Ma, *J. Mater. Sci.*, 2016, **51**, 9157–9189.
22 T. Li, M. Cao, M. Liang, J. Xie and G. Du, *Polymers*, 2017, **9**, 426.
23 H. Zhang, J. Feng, L. Li, Y. Jiang and J. Feng, *RSC Adv.*, 2019, **9**, 5967–5977.
24 T. He, Y. Zhang, Y. Chen, Z. Zhang, H. Wang, Y. Hu, M. Liu, C. W. Pao, J. L. Chen, L. Y. Chang, Z. Sun, J. Xiang, Y. Zhang and S. Chen, *J. Mater. Chem. A*, 2019, **7**, 20840–20846.
25 M. Salihovic, N. Hüsing, J. Bernardi, V. Presser and M. S. Elsaesser, *RSC Adv.*, 2018, **8**, 27326–27331.
26 Y. Luo, J. Wang, W. Lu, X. Wang, J. Yang, X. Zhang, Y. Xue, J. Wang and F. Yu, *Colloids Surf., A*, 2024, **702**, 134766.
27 S. S. Kenganal and A. Sahoo, *J. Energy Storage*, 2024, **78**, 109805.
28 C. Lin and J. A. Ritter, *Carbon*, 2000, **38**, 849–861.
29 G. Ramos-Fernández, M. Canal-Rodríguez, A. Arenillas, J. A. Menéndez, I. Rodríguez-Pastor and I. Martin-Gullon, *Carbon*, 2018, **126**, 456–463.
30 Z. Xiao, W. Zhou, N. Zhang, Q. Zhang, X. Xia, X. Gu, Y. Wang and S. Xie, *Small*, 2019, **15**, 1804779.
31 D. Lu, S. Liao, Q. Wei, X. Xiao and Q. Wang, *Cellulose*, 2022, **29**, 7431–7444.
32 X. Jiang, Z. Zhao, S. Zhou, H. Zou and P. Liu, *ACS Appl. Mater. Interfaces*, 2022, **14**, 45844–45852.
33 X. Zhang, F. Zhang, H. Li, X. Yan, X. Zhao, W. Shi, Y. Liu, X. Wang and B. Liu, *J. Alloys Compd.*, 2025, **1010**, 177282.
34 Y. Xue, L. Shi, X. Liu, J. Fang, X. Wang, B. P. Setzler, W. Zhu, Y. Yan and Z. Zhuang, *Nat. Commun.*, 2020, **11**, 1–8.

35 D. Mladenović, A. Mladenović, D. M. F. Santos, A. B. Yurtcan, Š. Miljanić, S. Mentus and B. Šljukić, *J. Electroanal. Chem.*, 2023, **946**, 117709.
36 B. Šljukić, C. E. Banks and R. G. Compton, *J. Iran. Chem. Soc.*, 2005, **2**, 1–25.
37 J. Wu, *Chem. Rev.*, 2022, **122**, 10821–10859.
38 N. Ramaswamy and S. Mukerjee, *Adv. Phys. Chem.*, 2012, 491604.
39 S. Liu, M. G. White and P. Liu, *J. Phys. Chem. C*, 2016, **120**, 15288–15298.
40 C. Hu and L. Dai, *Angew. Chem., Int. Ed.*, 2016, **55**, 11736–11758.
41 P. Li, Z. Jin and D. Xiao, *J. Mater. Chem. A*, 2014, **2**, 18420–18427.
42 J. Chmiola, P. L. T. Celine Largeot, P. Simon and Y. Gogotsi, *Science*, 2010, **328**, 480–483.
43 Y. Zhu, S. Murali, M. D. Stoller, K. J. Ganesh, W. Cai, P. J. Ferreira, A. Pirkle, R. M. Wallace, K. A. Cychosz, M. Thommes, D. Su, E. A. Stach and R. S. Ruoff, *Science*, 2011, **332**, 1537–1541.
44 P. G. Bruce, B. Scrosati and J. M. Tarascon, *Angew. Chem., Int. Ed.*, 2008, **47**, 2930–2946.
45 P. Poizot, S. Laruelle, S. Grugeon, L. Dupont and J. M. Tarascon, *Nature*, 2000, **407**, 496–499.
46 D. Guo, R. Shibuya, C. Akiba, S. Saji, T. Kondo and J. Nakamura, *Science*, 2016, **351**, 361–365.
47 C. Zhang, G. Liu, Q. Long, C. Wu and L. Wang, *J. Colloid Interface Sci.*, 2022, **622**, 849–859.
48 K. Artyushkova, A. Serov, S. Rojas-Carbonell and P. Atanassov, *J. Phys. Chem. C*, 2015, **119**, 25917–25928.
49 W. Peng, J. Liu, X. Liu, L. Wang, L. Yin, H. Tan, F. Hou and J. Liang, *Nat. Commun.*, 2023, **14**, 1–11.
50 E. Jung, H. Shin, W. Hooch Antink, Y. E. Sung and T. Hyeon, *ACS Energy Lett.*, 2020, **5**, 1881–1892.
51 Y. Pang, H. Xie, Y. Sun, M. M. Titirici and G. L. Chai, *J. Mater. Chem. A*, 2020, **8**, 24996–25016.
52 A. Olean-Oliveira, N. Hasnain, R. Martínez-Hincapié, U. Hagemann, A. Jain, D. Segets, I. Spanos and V. Čolić, *ACS Catal.*, 2024, **14**, 17675–17689.
53 T. W. Chen, S. M. Chen, G. Anushya, R. Kannan, P. Veerakumar, M. M. Alam, S. Alargarsamy and R. Ramachandran, *Nanomaterials*, 2023, **13**, 2012.
54 J. Yu, S. Giancola, B. Khezri, D. Nieto-Castro, J. Redondo, F. Schiller, S. Barja, M. C. Spadaro, J. Arbiol, F. A. Garcés-Pineda and J. R. Galán-Mascarós, *EES Catal.*, 2023, **1**, 765–773.
55 W. S. Freitas, P. P. M. Pico, A. D'epifanio and B. Mecheri, *Catalysts*, 2021, **11**, 1525.
56 J. Fernández-Vidal, L. J. Hardwick, G. Cabello and G. A. Attard, *Faraday Discuss.*, 2024, **248**, 102–118.
57 J. T. Bender, R. Y. Sanspeur, A. E. Valles, A. K. Uvodich, D. J. Milliron, J. R. Kitchin and J. Resasco, *ACS Energy Lett.*, 2024, **9**, 4724–4733.
58 F. Ni, K. Jia, Y. Chen, Y. Wen and S. He, *Mater. Chem. Front.*, 2023, **7**, 2750–2763.
59 K. Morawa Eblagon, N. Rey-Raap, J. L. Figueiredo and M. F. R. Pereira, *Appl. Surf. Sci.*, 2021, **548**, 149242.
60 L. Álvarez-Manuel, C. Alegre, D. Sebastián, A. Eizaguerri, P. F. Napal and M. J. Lázaro, *Catal. Today*, 2023, **418**, 114067.
61 L. Álvarez-Manuel, C. Alegre, D. Sebastián, P. F. Napal, C. Moreno, E. Bailón-García, F. Carrasco-Marín and M. J. Lázaro, *ChemElectroChem*, 2024, **11**, e202300549.
62 D. Mladenović, D. M. F. Santos, G. Bozkurt, G. S. P. Soylu, A. B. Yurtcan, Š. Miljanić and B. Šljukić, *Electrochem. Commun.*, 2021, **124**, 106963.
63 M. Shen, J. Qi, K. Gao, C. Duan, J. Liu, Q. Liu, H. Yang and Y. Ni, *Chem. Eng. J.*, 2023, **464**, 142719.
64 H. Li, X. Shu, P. Tong, J. Zhang, P. An, Z. Lv, H. Tian, J. Zhang and H. Xia, *Small*, 2021, **17**, 2102002.
65 Q. Li, Z. Sun, C. Yin, Y. Chen, D. Pan, B. Yu, Y. Zhang, T. He and S. Chen, *Chem. Eng. J.*, 2023, **458**, 141492.
66 S. Chang, H. Zhang and Z. Zhang, *J. Energy Chem.*, 2021, **56**, 64–71.
67 F. Chen, F. Yang, S. Che, H. Liu, C. Xu, N. Chen, Y. Sun, C. Yu, Z. Wu and Y. Li, *Green Chem. Eng.*, 2023, **4**, 365–375.
68 G. Fu, Y. Liu, Y. Chen, Y. Tang, J. B. Goodenough and J. M. Lee, *Nanoscale*, 2018, **10**, 19937–19944.
69 Y. Zhang, X. Zhang, Y. Li, J. Wang, S. Kawi and Q. Zhong, *Nano Res.*, 2023, **16**, 6870–6880.
70 J. S. M. Lee, T. H. Wu, B. M. Alston, M. E. Briggs, T. Hasell, C. C. Hu and A. I. Cooper, *J. Mater. Chem. A*, 2016, **4**, 7665–7673.
71 M. Samancı, E. Daş and A. Bayrakçeken Yurtcan, *Int. J. Energy Res.*, 2021, **45**, 1729–1747.
72 J. Á. Martín-Illán, L. Sierra, P. Ocón and F. Zamora, *Angew. Chem.*, 2022, **134**, e202213106.
73 V. Augustyn, P. Simon and B. Dunn, *Energy Environ. Sci.*, 2014, **7**, 1597–1614.
74 Y. Jiang and J. Liu, *Energy Environ. Mater.*, 2019, **2**, 30–37.
75 T. Schoetz, L. W. Gordon, S. Ivanov, A. Bund, D. Mandler and R. J. Messinger, *Electrochim. Acta*, 2022, **412**, 140072.
76 G. He, M. Qiao, W. Li, Y. Lu, T. Zhao, R. Zou, B. Li, J. A. Darr, J. Hu, M.-M. Titirici, I. P. Parkin, G. He, Y. Lu, T. Zhao, J. A. Darr, I. P. Parkin, M. Qiao, M. Titirici, W. Li, R. Zou, B. Li and J. Hu, *Adv. Sci.*, 2017, **4**, 1600214.
77 M. Zhang, D. Yang, S. Zhang, T. Xu, Y. Shi, Y. Liu, W. Chang and Z. Z. Yu, *Carbon*, 2020, **158**, 873–884.
78 M. T. Phong, C. V. Lam, N. T. T. Xuan, T. T. Trinh, N. H. K. Duyen, D. N. C. Vy, N. T. Son and P. M. Tu, *J. Appl. Electrochem.*, 2024, **54**, 1333–1348.
79 Y. J. Lee, J. C. Jung, S. Park, J. G. Seo, S. H. Baeck, J. R. Yoon, J. Yi and I. K. Song, *Curr. Appl. Phys.*, 2010, **10**, 947–951.
80 Q. Tian, F. Xiao, H. Zhao, X. Fei, X. Shen, G. Postole and G. Zhao, *Appl. Catal., B*, 2020, **272**, 119039.
81 Q. Ye, T. N. Hunter, H. Xu, D. Harbottle, G. M. Kale and M. R. Tillotson, *Sep. Purif. Technol.*, 2025, **353**, 128436.
82 J. H. Kim, Y. T. Kim and S. H. Joo, *Curr. Opin. Electrochem.*, 2020, **21**, 109–116.
83 Hydrogen Peroxide Market Size to Hit Around USD 11.54 Bn by 2034, **https://www.precedenceresearch.com/hydrogen-peroxide-market**, (accessed 21 February 2025).
84 S. C. Perry, S. Mavrikis, L. Wang and C. Ponce de León, *Curr. Opin. Electrochem.*, 2021, **30**, 100792.
85 Y. Yi, L. Wang, G. Li and H. Guo, *Catal. Sci. Technol.*, 2016, **6**, 1593–1610.
86 J. M. Campos-Martin, G. Blanco-Brieva and J. L. G. Fierro, *Angew. Chem., Int. Ed.*, 2006, **45**, 6962–6984.
87 S. Yang, A. Verdaguer-Casadevall, L. Arnarson, L. Silvioli, V. Čolić, R. Frydendal, J. Rossmeisl, I. Chorkendorff and I. E. L. Stephens, *ACS Catal.*, 2018, **8**, 4064–4081.
88 S. C. Perry, D. Pangotra, L. Vieira, L. I. Csepei, V. Sieber, L. Wang, C. Ponce de León and F. C. Walsh, *Nat. Rev. Chem.*, 2019, **3**, 442–458.
89 M. Melchionna, P. Fornasiero, M. Prato, M. Melchionna, P. Fornasiero and M. Prato, *Adv. Mater.*, 2019, **31**, 1802920.
90 L. Liang, M. Zhou, X. Lu, P. Su and J. Sun, *Electrochim. Acta*, 2019, **320**, 134569.